Applied Physics B (2021) 127:30
https://doi.org/10.1007/s00340-021-07578-w

Applied Physics B
Lasers and Optics

Comprehensive optimization of electronic and optical properties of polar III-nitride laser

Md Mobarak Hossain Polash[1,2] · Saumya Biswas[3] · M. Shah Alam[4]

Received: 24 November 2019 / Accepted: 15 January 2021 / Published online: 5 February 2021

Abstract
A detailed investigation is performed to obtain optimized optical performance of polar III-nitride single quantum well (SQW) semiconductor lasers by band engineering through symmetric and asymmetric tuning of device parameters. Electronic, optical, and threshold characteristics are calculated to analyze the effects of band engineering on device performance. Here, the InN-$In_{0.25}Ga_{0.75}$ N SQW structure is chosen as a case study. This work shows a significant improvement in optical properties from higher wavefunction overlap integral obtained from band modification due to the tuning which also provides higher momentum matrix elements, spontaneous emission rate, and optical gain, as well. The maximum TE-polarized optical gain for the symmetric structure is found as around 6291 cm^{-1} for 6 Å well width and 6 Å barrier width at 710 nm, while for asymmetric laser structure, a maximum TE-polarized optical gain of around 6225 cm^{-1} at around 800 nm is observed for 6 Å well width with asymmetric barrier width of 6 Å and 8 Å. The optimization is carried out over 500–1600 nm wavelength range to obtain the optimum structure for maximum optical performance at different wavelengths. A time-efficient genetic algorithm-based optimization is also performed that provides the same optimization results in reduced time.

1 Introduction

Nitride semiconductor LEDs and lasers are extensively studied for a long time as optoelectronics devices [1–3], energy-saving solid-state lighting sources [4–6], and next-generation display modules [7, 8]. Till now, most of the nitride LEDs and lasers are grown along the *c*-plane of wurtzite lattice [9–11], a hexagonal crystal system. The *c*-plane structures are also known as polar structures due to the presence of spontaneous and piezoelectric polarization within the heterostructure layers [9–12]. This total polarization from the lattice mismatch between the layers creates an internal electric field which minimizes the radiative recombination rate and optical gain of systems, caused quantum-confined Stark effect (QCSE) and redshift in emission spectra due to lower electron–hole wavefunction overlap integral factor ($\Gamma_{e\text{-}hh}$) [9–12]. Therefore, the *a*-plane semipolar and *m*-planes nonpolar semiconductor devices got huge attention recently [13–16]. Due to the absence of polarization-induced internal electric field in semipolar and nonpolar devices, higher radiative recombination rate and higher optical gain can be achieved from higher $\Gamma_{e\text{-}hh}$ [9–12].

Despite the opportunities of semipolar and nonpolar LEDs and lasers, they have unique challenges like dislocation-free layers growth by minimizing stress, indium uptakes in InGaN QW structures grown in MOCVD, a higher probability of impurity incorporation, and developing high-quality facets and ohmic contacts [9, 10, 14–16]. Therefore, it would be pivotal to achieve maximum performance from the commercially available *c*-plane LEDs and laser structures. Better performance in *c*-plane lasers can be achieved by maximizing $\Gamma_{e\text{-}hh}$ by engineering the band structure of the devices [17–19]. Generally, the band structure and, hence, the wave function of quantum structures can be engineered either by changing the material systems or by tuning the external device parameters like well width, barrier width, injection current density, and temperature [17–19], which can essentially tune $\Gamma_{e\text{-}hh}$ and hence the optical properties of laser

✉ Md Mobarak Hossain Polash
mhpolash@ncsu.edu

[1] Department of Materials Science and Engineering, North Carolina State University, Raleigh, NC 27606, USA

[2] Department of Electrical and Computer Engineering, North Carolina State University, Raleigh, NC 27606, USA

[3] Department of Physics, University of Oregon, Eugene, OR 97403, USA

[4] Department of Electrical and Electronic Engineering, Bangladesh University of Engineering and Technology, Dhaka, BD 1205, USA

structures. In this work, our main objective is to optimize the optical performance of the polar-nitride lasers by maximizing the $\Gamma_{\text{e-hh}}$ from the band engineering by tuning the external device parameters. We showed the general trends of laser performance as a function of the variation of those parameters at room temperature. It is observed that $\Gamma_{\text{e-hh}}$ can be significantly varied by tuning the device parameters as well as material compositions [17] which can provide higher optical gain from higher radiative recombination rate in the active region [18, 19]. The study of the threshold characteristics is also included to analyze the effects of change in device parameters.

In this work, a simulation model is developed to calculate electronic band properties as well as optical properties based on the mathematical models discussed in Sect. 2. A case study based on InN-InGaN SQW laser structure is presented as InN lasers cover a wide range of wavelength which is suitable for light sources in optical communication [20–22]. Here, it is important to note that the case structure is chosen from the previous literature neither for reproducing the results nor for optimizing the optical performance of that structure. Any nitride laser structure can be considered for the study, but here, previously published laser structure assists us to cross-check the results during the study of tuning device parameters. Section 3 presents the variation of the electronic band properties mediated by device parameters. The effects of the tuning of the device parameters on the optical properties are discussed in Sect. 4. Section 5 demonstrates the variation in threshold characteristics for the variation of device parameters. Section 6 presents the comparative study of the optical properties for the state-of-the-art. A time-efficient genetic-algorithm-based optimization process is shown in Sect. 7. From this detailed investigation, it is observed that a significant improvement in optical properties can be achievable for *c*-plane nitride lasers from band engineering by tuning the device parameters.

2 Numerical formalism for simulation model

The electronic band structure of the *c*-plane wurtzite-nitride device is calculated from the standard Hamiltonians. Effective mass approximation and parabolic band nature are considered for calculating conduction bands, while hole wave functions are calculated considering valence band mixing effect, strain effect from lattice mismatch, carrier screening effect, and spontaneous and piezoelectric polarization effect-induced internal electric field [23–27]. Deformation potentials are utilized to integrate strain effects which cause band edge shifting in conduction and valence bands, respectively [28]. The considered conduction band Hamiltonian is [23–27]:

$$H^c(k_t,k_z)=\frac{\hbar^2}{2}\left(\frac{k_t^2}{m_e^t}+\frac{k_z^2}{m_e^z}\right)+E_c^0(z)+P_{c\varepsilon}(z), \tag{1}$$

where k_t and k_z are the wave vectors perpendicular (t) and parallel (z) to the growth direction (c-axis),m_e^t and m_e^z are the electron effective masses in t- and z-direction, respectively, and $P_{c\varepsilon}(z)$ is hydrostatic band shift due to the strain effect [21]. The spontaneous polarization is determined by linear interpolation [24, 25]. The piezoelectric polarization is obtained from the piezoelectric coefficient and elastic stiffness coefficients [29]. The periodic boundary condition is applied to ensure zero average electric field in the layers [23, 24].

The internal electric field of nitride devices is always screened by the sheet carrier density accumulated at nitride interfaces [21]. Therefore, the carrier screening effect can modify the electronic band structure which is incorporated into a self-consistent model [21]. Higher carrier density gives higher energy band modification [21]. The 6 × 6 diagonalized ***k.p*** Hamiltonian for hole structure [23–27] that considered into this model is:

$$H_{6\times6}^v(k)=\begin{bmatrix}H_{3\times3}^U(k) & 0\\ 0 & H_{3\times3}^L(k)\end{bmatrix}, \tag{2}$$

where ${H_{3\times3}}^U$ and ${H_{3\times3}}^L$ are 3 × 3 upper and lower Hamiltonian matrices defined in [23–27].

The TE- and TM-polarized interband transition matrix elements are calculated from the electronic band structures to obtain the optical properties [23–25]. Calculation of transition matrix elements includes all possible transitions between confined electron and hole energy bands due to the breaking of the orthogonality condition arising from polarization field-induced band bending in III-Nitride QW [30, 31]. Based on the Fermi's Golden rule, the spontaneous emission rate for TE or TM polarization is obtained as [23–27]:

$$g_{sp}^e(\hbar\omega)=\frac{q^2}{c\varepsilon_0 m_0^2\omega n_r L_w}\sum_{\sigma=U,L}\sum_{n,m}\int k_t dk_t \\ |(M_e)_{nm}(k_t)|^2\frac{f_n^c(k_t)(1-f_m^v(k_t))(\gamma/\pi)}{(E_{nm}^{cv}(k_t)-\hbar\omega)^2+\gamma^2}, \tag{3}$$

where e is the polarization vector, q is the electron charge, c and ε_0 are the speed of light and permittivity in free space, m_0 is the free-electron mass, n_r is the refractive index, L_w is the well width of the quantum well, $M_{nm}(k_t)$ is the momentum matrix or interband transition matrix elements at k_t between nth and mth energy level, f is the Fermi–Dirac distribution function, and $\hbar\gamma$ is the half linewidth of the Lorentzian function. The optical gain is then calculated from the spontaneous emission rate [23–27] using:

$$g(\hbar\omega) = g_{sp}^{e}(\hbar\omega)\left[1 - \exp\left(\frac{\hbar\omega - \Delta F}{k_B T}\right)\right]. \quad (4)$$

The separation of the quasi-Fermi levels, ΔF, is injection carrier density-dependent [23]. The total spontaneous emission rate per unit volume-energy interval is calculated from [23–27]:

$$r_{sp}(\hbar\omega) = \frac{n_r^2\omega^2}{\pi^2\hbar c^2}\frac{2(2g_{sp}^{x} + g_{sp}^{z})}{3}. \quad (5)$$

The total spontaneous emission rate per unit volume can be obtained from (6) using the following relationship [23, 24]:

$$R_{sp} = \int_0^\infty r_{sp}(\hbar\omega)d(\hbar\omega). \quad (6)$$

Radiative recombination current density is defined as $J_{\text{rad}} = qdR_{sp}$, where d is the length of the active region [23, 24]. The threshold characteristics of a laser structure are generally related to the geometry and materials of the structure [21]. The threshold gain is calculated from $\Gamma_{\text{opt}}g = \alpha_i + \alpha_m$ [21], where Γ_{opt} is the optical confinement factor, α_i and α_m are the internal loss and mirror loss, respectively, and g is optical gain. To obtain the threshold current density (J_{th}), the non-radiative current density component is calculated from monomolecular current ($J_{mc} = Aqdn$) and Auger current densities ($J_{ac} = Cqdn^3$), where A is monomolecular recombination constant and C is Auger coefficient [17, 21]. Total recombination consists of both radiative and non-radiative recombination components [17]. Therefore, total recombination current density is $J_{\text{tot}} = J_{\text{rad}} + J_{mc} + J_{ac}$.

3 Tuning of electronic properties

The analysis is performed on c-plane (0001) InN-$In_{0.25}Ga_{0.75}$ N laser structure with GaN separate confinement heterostructure (SCH). This nitride structure covers a wide range of wavelengths (500 nm–1600 nm) [32] which can be a prospective optical source for communication [21, 22, 33, 34]. Typical symmetric and asymmetric InN laser structures are shown in the insets of Fig. 1 where the well layer is InN with barrier layers of $In_{0.25}Ga_{0.75}$ N and an SCH of GaN. In this study, both well and barrier layer widths are varied with 2 Å step size from 3 Å to 20 Å. SCH width is varied in a way to keep the total device length 150 Å, but SCH variation has an insignificant impact on optical properties. Injection carrier density, the carriers recombined radiatively in the active region [21], is varied from 5×10^{18} cm^{-3} to 5×10^{19} cm^{-3}. The temperature and material compositions are kept fixed. Though, the variation of the composition of barrier materials can also be utilized to tune the laser properties [17].

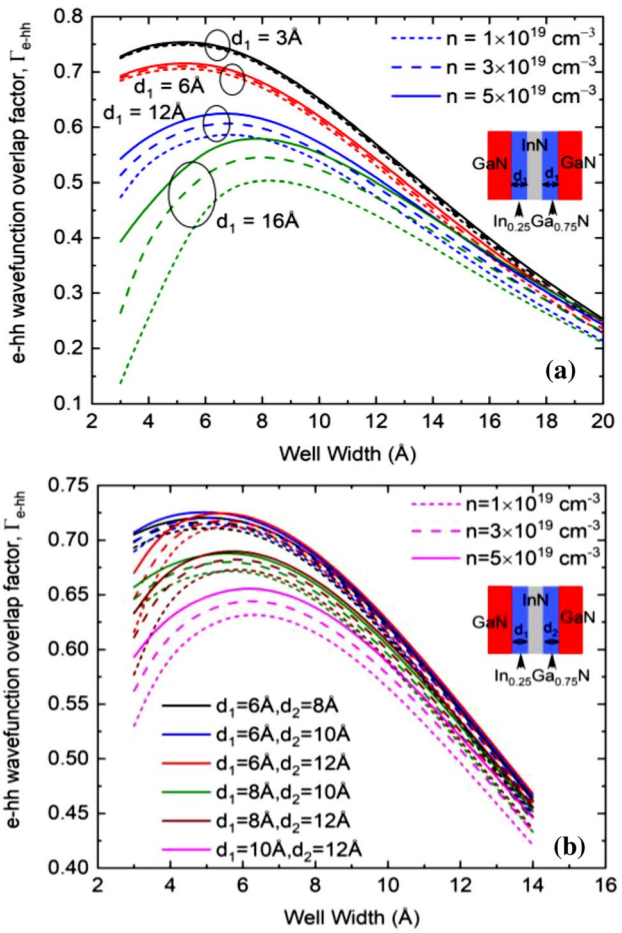

Fig. 1 Electron–hole (e-hh) wavefunction overlap integral factor ($\Gamma_{\text{e-hh}}$) of **a** symmetric and **b** asymmetric InN/ $In_{0.25}Ga_{0.75}$ N QW structure with different barrier width as a function of well width at different carrier densities

As mentioned earlier, the e-hh wavefunction overlap factor ($\Gamma_{\text{e-hh}}$) is a pivotal parameter for optimizing the device performance, an analysis is performed to observe the change in $\Gamma_{\text{e-hh}}$ for the symmetric and asymmetric variation of device parameters which is illustrated in Fig. 1.

For simplicity, a few higher $\Gamma_{\text{e-hh}}$ values are shown for both symmetric and asymmetric structures. As seen in both figures, symmetric and asymmetric tuning of device parameters can significantly improve $\Gamma_{\text{e-hh}}$ comparing with prior results [21, 34] which indicates that band engineering by tuning device parameters can introduce beneficial band structure modification. The highest obtained value for $\Gamma_{\text{e-hh}}$ is 76% for symmetric device structure with a 3 Å barrier and 6 Å well layer, while an asymmetric structure with 6 Å well, 6 Å and 10 or 12 Å barrier, and 55 Å and 71 Å SCH layers

give the highest overlap of 73% between electron and hole wavefunctions at 5×10^{19} cm^{-3} carrier density. According to Fig. 1, laser structure with shorter barrier layers shows less variation to the change in carrier density which can cause lower radiative recombination in active region at higher carrier density and hence reduce the optical gain. The impact of shorter barrier layers on optical gain can be understood from the optical gain behavior with respect to the variation of the device parameters. Trends in $\Gamma_{\text{e-hh}}$ observed in Fig. 1 have good agreement with previous results [32].

To show the impact of the tuning on band profile, band structures are calculated for two different symmetric device parameters and two asymmetric device parameters, respectively. Figure 2 shows the band profile of both symmetric and asymmetric devices along with the corresponding electron and heavy-hole wavefunctions, respectively. The slope in the band edge of the laser structure is arising from the internal electric field due to polarization which reduces

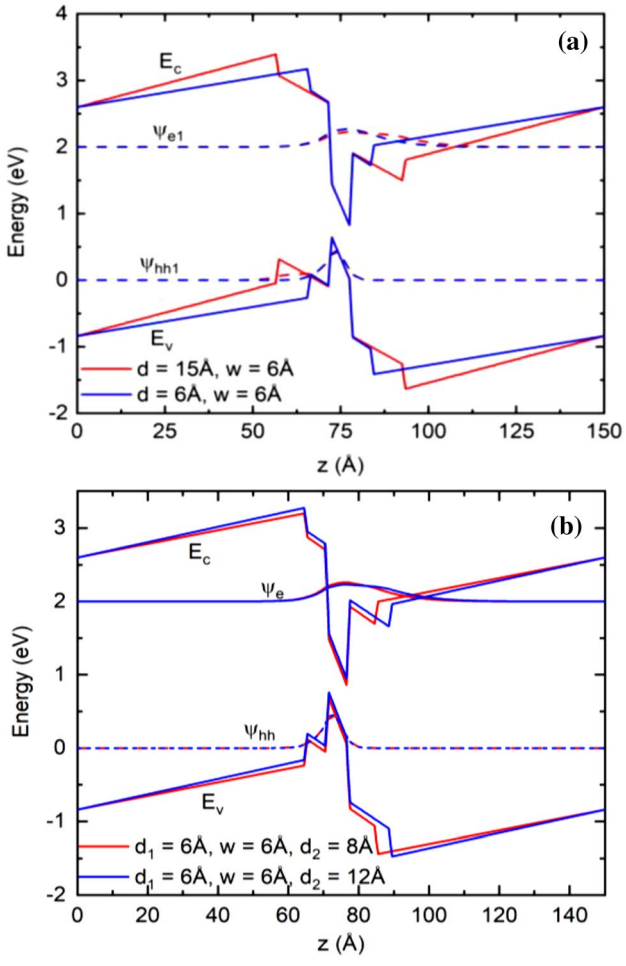

Fig. 2 **a** Symmetric and **b** asymmetric InN/ $In_{0.25}Ga_{0.75}$ N QW structures along with corresponding electron (e1) and heavy-hole (hh1) wavefunctions at 5×10^{19} cm^{-3} carrier density and 300 K

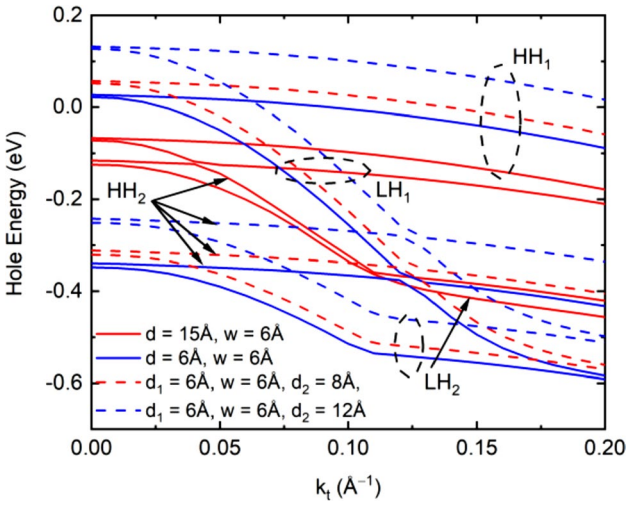

Fig. 3 Hole energy subbands of 4 different InN/ $In_{0.25}Ga_{0.75}$ N QW structures as a function of in-plane wavenumber (k_t) at 5×10^{19} cm^{-3} carrier density

overlapping between electron and hole wavefunctions (seen in Fig. 2).

As seen in Fig. 1, devices with thinner well and barrier width gives higher $\Gamma_{\text{e-hh}}$. But also, a thinner active region gives less radiative recombination hence less optical gain from lower optical confinement factor. To get more insight into energy band modification, electronic energy bands are also calculated for the devices, as shown in Fig. 2. Figure 3 illustrates only hole energy bands, as hole energy bands have valence bands mixing effects and show significant modifications due to the tuning of the device parameters. Here, the first four-hole energy bands are shown in band profile, i.e., HH1, LH1, HH2, and LH2 (HH—heavy hole and LH—light hole) as a function of the in-plane wave vector (k_t). The nature of hole subbands is determined depending on the contribution of the bulk valence bands. HH and LH have almost the same effective masses at the zone center ($k_t=0$), while LH effective mass becomes lower than that of HH at far away from the zone center. It is seen in Fig. 3 that all device structures show similar trends in electronic band structures. However, the wider structure has narrower energy-spacing between bands, and also bands are shifted toward higher hole energy. Moreover, variation in the single barrier layer in the asymmetric device shifts the bands toward higher energy. Observed trends in band structure modification due to tuning can be related to the internal electric field created due to polarization.

Figure 2 shows that wider device structures have a higher internal electric field which can cause shifting in the band structure. Also, according to the device physics theory, a wider device has narrower band spacing which is seen in Fig. 3. According to the observed trends in band structures in Fig. 3, it is expected that with an increase in width of the

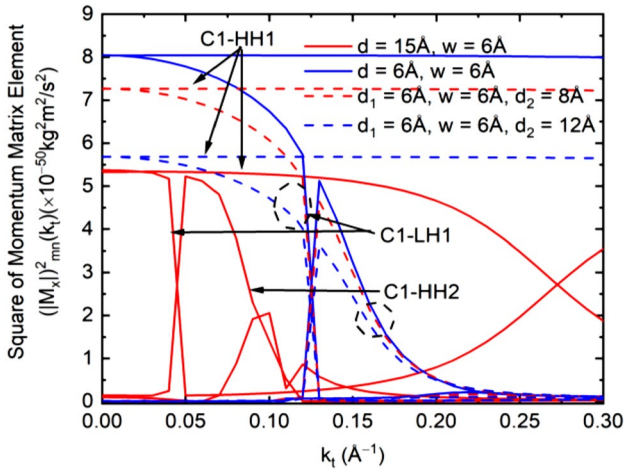

Fig. 4 TE-polarized momentum matrix elements of both symmetric and asymmetric InN/$In_{0.25}Ga_{0.75}$ N QW with GaN SCH layer for 5×10^{19} cm^{-3}

active layer, peak emission wavelength will increase, while Figs. 1 and 2 suggest that wider structures have less overlap between e–hh wavefunctions causing a reduction in optical gain. Here, it is mention-worthy that the active region for a laser structure contains well and barrier layers. With the increase in injection carrier density, the band bending and radiative recombination rate increase due to the carrier screening effect.

4 Tuning of optical properties

To understand the effects of the tuning on optical properties, a detailed calculation is performed on various optical properties of the laser structure. From obtained electronic band structures, optical transition matrix elements are calculated for the devices given in Fig. 2. Figure 4 demonstrates the TE-polarized momentum or optical transition matrix elements as a function of in-plane wavenumber at 5×10^{19} cm^{-3} and 300 K. TM-polarized transition matrix elements are significantly weaker than TE-polarized matrix elements. Since the compressive strain in the quantum well makes the top valence subbands HH- or LH-like, the dominant transitions for this structure are TE polarized [21]. Among different kinds of TE-polarized optical transitions (C_n-HH/LH_m: the transition between nth conduction band to mth heavy/light hole band), only three dominated transitions are shown in Fig. 4, i.e., C1-HH1, C1-LH1, and C1-HH2. According to the dispersion relation of the square of the momentum matrix elements shown in Fig. 4, C1-HH1 and C1-LH1 have strong TE components near the zone center ($k_t=0$) where C1-HH1 remains strong at the far region from the zone center and C-LH1 decays gradually. The C1-HH2 shows good improvement only in the far region from the zone center. C1-HH1 and C1-LH1 contribute significantly to the spontaneous emission rate and optical gain of the structure. Moreover, a laser device with a wider active region has weaker transition matrix elements compare to that of a thinner active region which can be related to the electronic band structure. As mentioned earlier, e-hh wavefunctions have lower overlap in the wider device due to the internal electric field which lowers the probabilities of optical transitions and hence reduces the strength of matrix elements. The observed trends in optical transition matrix elements follow the trends of electronic band structures, as shown in Fig. 2.

For laser devices, optical transition matrix elements contribute to producing spontaneous emission in the gain medium which eventually gives the optical output. Therefore, spontaneous emission rate spectra are calculated from

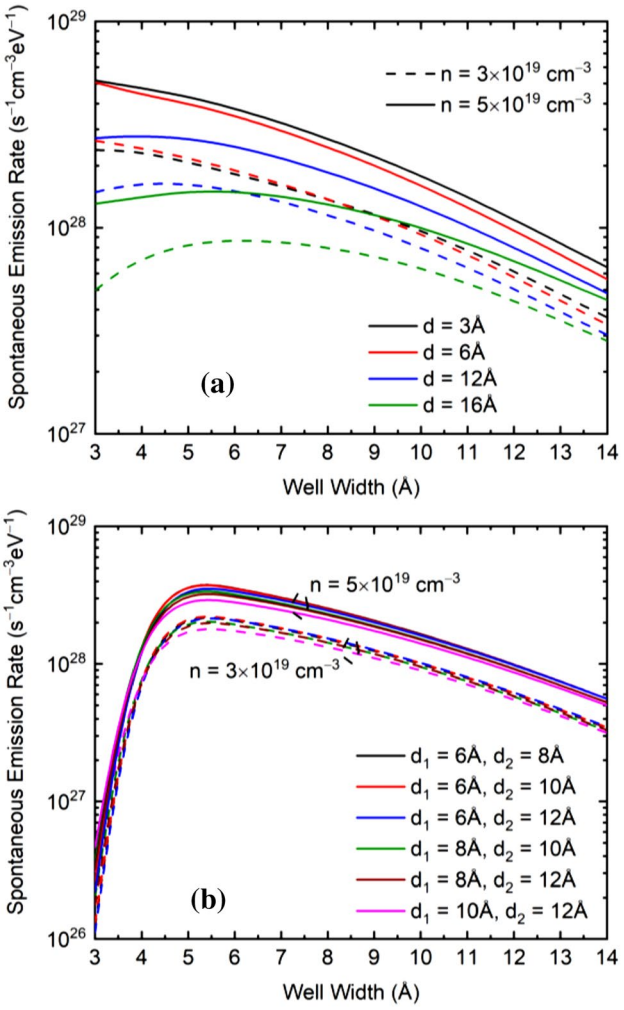

Fig. 5 Peak spontaneous emission rate as a function of well width for **a** symmetric device structure and **b** asymmetric device structure with different barrier width at different carrier densities of 3×10^{19} cm^{-3} and 5×10^{19} cm^{-3}

the dispersion relation for both symmetric and asymmetric device structures, and peak emission rate spectra are shown in Fig. 5 as a function of well width. As the spontaneous emission rate is calculating from optical transition matrix elements, the spontaneous emission rate is higher for the laser structure with a thinner active region where interband optical transition probability is higher due to the higher overlap factor. Here, the asymmetric device structure with 6 Å barrier width shows a good improvement in the emission rate. The reason behind observing improved emission rate peak for device structure with 6 Å barrier width is the contribution of emission rate as well as the volume of the active region.

Due to the trade-off between these two parameters, an intermediate structure between thinner and wider device structure shows better performance in terms of generating spontaneous emission. Figure 5b only demonstrates the emission rate of asymmetric devices with a higher overlap factor. According to the figure, all device structures show almost similar trends in spontaneous emission rate. Here, the peak spontaneous emission rate is shown for 3×10^{19} cm^{-3} and 5×10^{19} cm^{-3} carrier densities at $T=300$ K. From the calculated spontaneous emission rate, optical gain is determined for the given device structures of Fig. 5. For better illustration, Fig. 6 illustrates the trends in peak optical gain of the laser devices for only 5×10^{19} cm^{-3} carrier densities at $T=300$ K, as the optical gain is stronger at higher carrier densities.

Trends in optical gain from Fig. 6 also show that a different device has better optical gain than the device with a higher overlap factor. The key factor is the stimulated emission occurring in the active region. As in the Fabry–Perot laser systems, the spontaneous emission spectra provide required stimulated emission to generate lasing with the help of reflective ends, it is expected that the structure having higher spontaneous emission should provide higher stimulated emission and hence higher optical gain. Here, the symmetric device structure with $d=6$ Å and $w=6$ Å has the highest optical gain at $T=300$ K which is around 6291 cm^{-1}, whereas an asymmetric device with $d_1=6$ Å, $d_2=8$ Å and $w=6$ Å gives the highest optical gain of 6225 cm^{-1}. Figure 6 also demonstrates the variation in peak emission wavelength due to device parameters tuning which shows a good agreement with the previous result [32]. It is observed in Fig. 6 that the thinner active region has a lower optical gain which corresponds to a lower recombination rate occurring in the active region. Figure 6 demonstrates the optimized optical gain performance with their peak emission wavelength for corresponding devices.

Figure 7 demonstrates the optical gain spectra as a function of photon energy for the device structures of Fig. 4 at 3×10^{19} cm^{-3} and 5×10^{19} cm^{-3} carrier densities. Observed optical gain spectra in Fig. 7 have good agreement with

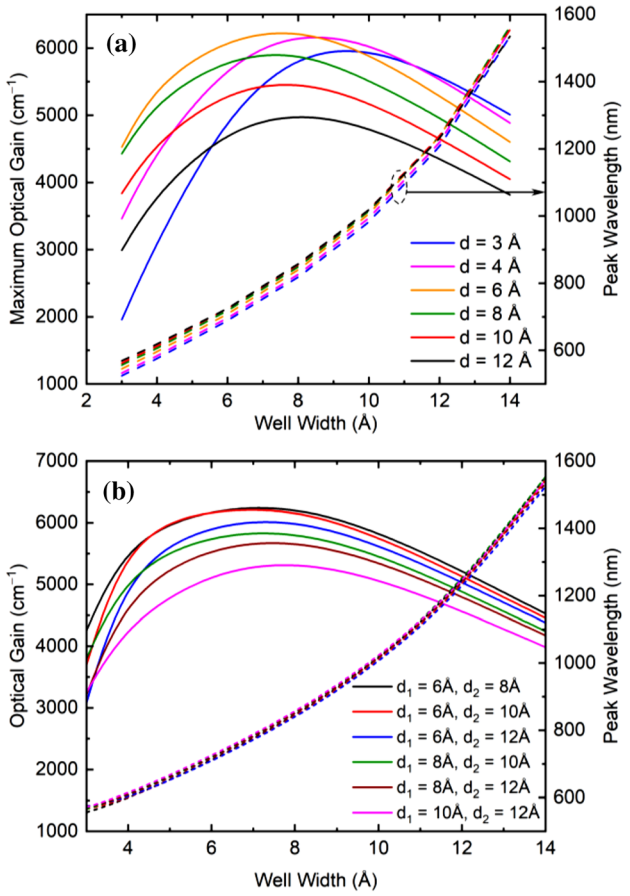

Fig. 6 Peak TE-polarized optical gain and corresponding peak emission wavelength as a function of well width for **a** symmetric device structure and **b** asymmetric device structure with different barrier width at 5×10^{19} cm^{-3}

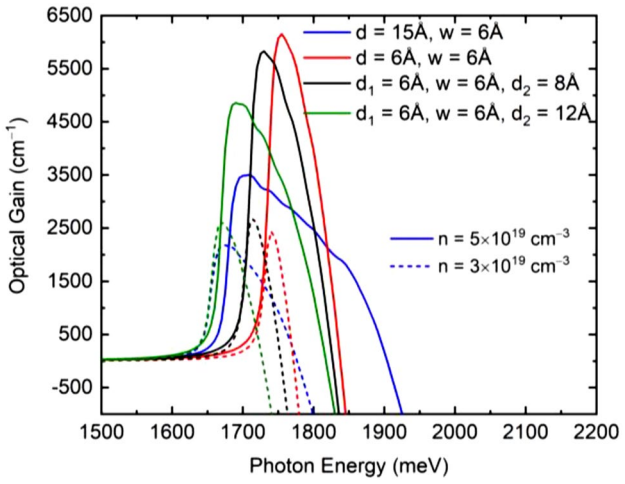

Fig. 7 TE-polarized optical gain spectra of symmetric and asymmetric InN/$In_{0.25}Ga_{0.75}$ N QW structures with different device parameters for carrier density of 3×10^{19} cm^{-3} and 5×10^{19} cm^{-3}

the optical gain, as shown in Fig. 6. According to Fig. 7, laser structures with the thinner active region have a narrow range of lasing wavelength and in general, peak emission wavelength shows a blue shift with the increase in carrier density. Also, peak optical gain increases significantly with the increase in carrier density. Typically, higher carrier density gives a higher emission rate due to higher wavefunction overlap factor, while causes the blue shift due to higher carrier screening effect.

To analyze the laser performance as an optical source, it is important to determine the radiative recombination occurring inside the active region. As mentioned, the active region has both radiative and non-radiative recombination and only radiative recombination gives effective lasing; therefore, higher radiative recombination means higher efficiency in lasing action. Radiative recombination rate per unit volume (R_{sp}) is calculated for different carrier densities (5×10^{18} cm^{-3} to 5×10^{19} cm^{-3}) and the results are illustrated in Fig. 8. Here, the radiative recombination rate as a function of carrier density is shown for only four laser structures used in other figures. Generally, the radiative recombination rate is lower at a lower range of carrier density which is usable for LED operation, while a higher range of carrier density provides a higher recombination rate that useful for laser devices. Also, a higher e–hh overlap factor helps to provide higher radiative recombination in the active layers. It is seen from Fig. 8 that laser structure with a narrower active region has a higher radiative recombination rate at higher carrier densities than laser structures with a wider active region which corresponds to the observed trends in the electronic band structure and e-hh overlap factor. Significant growth in radiative recombination is observed above 3×10^{19} cm^{-3} carrier density for all the devices. This radiative recombination rate is later utilized to determine the threshold characteristics of the laser devices.

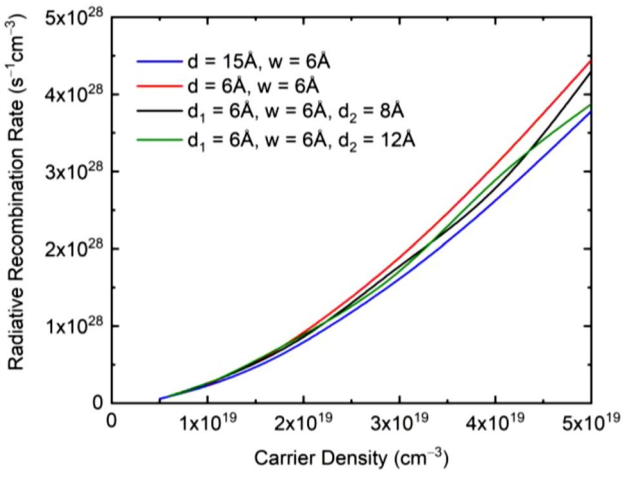

Fig. 8 Radiative recombination rate versus carrier density at 300 K for different symmetric and asymmetric laser devices

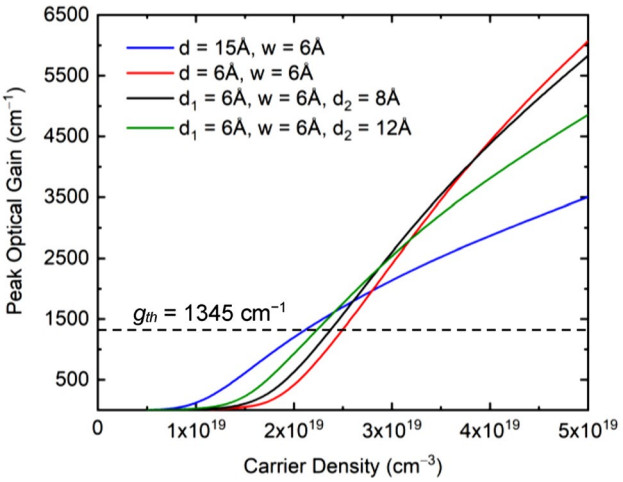

Fig. 9 Peak TE-polarized optical gain of symmetric and asymmetric InN/$In_{0.25}Ga_{0.75}$ N QW lasers as a function of carrier density

Like the variation of radiative recombination rate with respect to carrier density, optical gain versus carrier density behavior also provides an important understanding of the device operation. Therefore, peak optical gain is demonstrated in Fig. 9 as a function of carrier density for the defined laser structures. Figure 9 shows some interesting features about laser structure performance with respect to injection carrier densities. At lower carrier densities (suitable operating range for LEDs), a device with wider active layers gives a better optical gain performance, while at higher carrier densities, devices with narrower active regions perform better. Moreover, the transparency carrier density is lower for a wider active region than that of a wider active region. Here, transparency carrier density refers to the carrier density at which laser gain equals the loss components of the laser. This indicates that for the devices with a wider active region, lower carrier density can compensate the loss components faster than that of the devices with a narrower active region. As seen in Fig. 8, at lower carrier densities, radiative recombination rates are equals for different device structures, optical gain at lower carrier densities for laser structure with the wider active region may be benefited from the higher volume of an active region.

Based on Figs. 8 and 9, peak optical gain is calculated as a function of radiative current density for the reference structures and demonstrated in Fig. 10. It is seen that at a radiative current density above 25 Acm^{-2}, the laser structures show significant growth in optical gain with the increase in current density. The laser structures with a wider active region need higher radiative current density to achieve its highest optical gain. In terms of utilized radiative current density for lasing, laser structures with narrower active

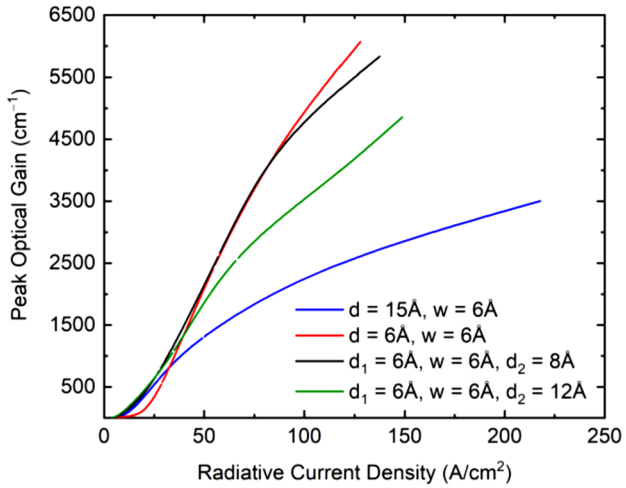

Fig. 10 Peak optical gain of symmetric and asymmetric InN/$In_{0.25}Ga_{0.75}$ N QW structures as a function of radiative recombination current density

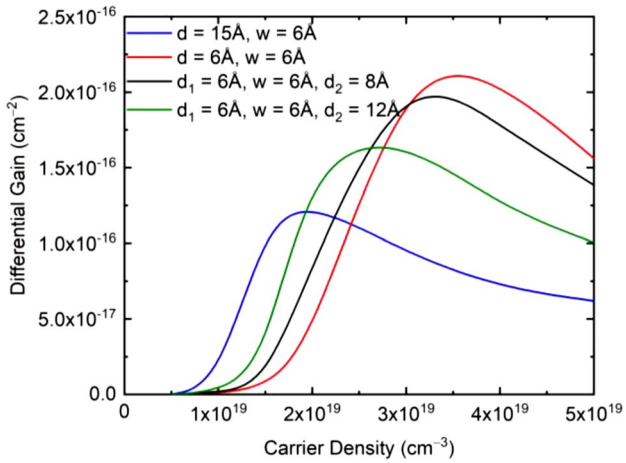

Fig. 11 Differential gain of InN/$In_{0.25}Ga_{0.75}$ N QW with GaN layers as a function of carrier density from 5×10^{18} cm^{-3} up to 5×10^{19} cm^{-3}

regions show better performance, as they can provide more gain with lower current density input. The current density at which lasing starts is lower for wider active region structures that agree with the previous figure. To understand the efficient performance of the laser devices, details on threshold characteristics need to be studied which is discussed in the following section.

Finally, differential gain (dg/dn) is calculated for the reference structures and illustrated in Fig. 11 as a function of carrier density. Differential gain refers to the growth rate of optical gain for injection carrier density [21]. Typically, for a laser structure, differential gain shows increasing nature at lower carrier densities primarily due to the carrier screening effect, then reaches the optimum value, and starts decreasing with the increase in carrier density mainly due to the band filling effect. As seen in Fig. 11, all the devices show typical differential gain behavior with respect to carrier density as mentioned. Laser structures with narrow active regions show sharper increment in differential gain at comparatively higher carrier density. However, device structures with wider active layers show good improvement at lower carrier density and saturate early due to higher carrier screening effect. This behavior is also attributed to the trends seen in Fig. 9. According to Fig. 9, device structures with narrower active region suffer less from the carrier screening effects due to lower induced internal electric field in the heterostructure layers which has good agreements with the previous discussions of Sect. 3 and Sect. 4.

5 Impact of tuning on threshold characteristics

To study the threshold characteristics for device parameters tuning, we consider a Febry–Perot Laser system with SQW mentioned in Section III. For the calculation, the laser cavity length is considered as 650 μm and end-facet reflectivities are 95% and 56%. Here, the laser cavity includes the reflective mirror systems, SCH layers, and the active region. As the total cavity length is much higher than the active region length, the cavity length is kept fixed in the model. Two optical confinement factors (Γ_{opt}) are considered as 0.01 (1%) [23] and 0.005 (0.5%). Here, it is important to mention that the optical confinement factor of 0.01 is considered due to the similar nitride laser structure reported in the previous literature [23]. As the practical confinement factor can be lower than the considered value for an active layer of several angstroms, we also considered another lower confinement factor. Generally, the confinement factor of a VCSEL structure depends on the optical mode and the thickness of the optical cavity. Here, we did not perform the calculation of the optical mode for the nitride VCSEL structure, as our main focus is to study the impact of the tuning parameters on the optical performance and, hence, the threshold properties. Therefore, we chose the confinement value from the previous literature that presented a similar device structure. We analyzed the impact of tuning the external device parameter on the threshold characteristics. Among the other considered parameters, the internal loss (α_i) is taken as 8.6 cm^{-1} and the mirror loss (α_m) is calculated as 4.85 cm^{-1} from the values of reflectivities. From (8), the threshold gain are found as 1345 cm^{-1} (for $\Gamma_{opt}=0.01$) and 2690 cm^{-1} (for $\Gamma_{opt}=0.005$). The threshold carrier density (n_{th}) can be determined for different laser structures from Fig. 9. As seen in Fig. 9, for 1% optical confinement factor, the threshold carrier density is lower for the laser with a wider active region that similar to the trends seen for transparency carrier density, while the

wider symmetric active layer exhibits higher threshold carrier concentration for lower optical confinement factor. As mentioned, to determine the efficiency of the laser device performance, it is important to calculate the total operating current density and corresponding threshold current densities for corresponding devices. According to the formula given in Section II, the total current density can be determined from radiative and non-radiative current density components. From Figs. 8 and 10, radiative recombination current density can be obtained. To calculate the other components of the total current density, both monomolecular current density and Auger current densities component are calculated based on the formula given in Sect. 2.

Typically, the wide band-gap QW structures have a negligible contribution from the Auger recombination. However, InN QW structures have a small bandgap, and the Auger current density is calculated from $C = 1 \times 10^{-32}$ $cm^6 s^{-1}$ and $C = 1 \times 10^{-31}$ $cm^6 s^{-1}$ [35–37]. For calculating monomolecular current density, different values of A are considered as 6×10^8, 1×10^9, and 1.5×10^9 s^{-1} [21]. Figure 12 demonstrates the total current density and corresponding peak optical gain as a function of different barrier layers for symmetric and asymmetric laser structures with three different well widths of 3 Å, 6 Å, and 9 Å at 5×10^{19} cm^{-3} carrier density, $A = 1 \times 10^9$ s^{-1}, and $C = 1 \times 10^{-31}$ $cm^6 s^{-1}$. Both symmetric and asymmetric structures show increment in total current density with the increase in device length. For obtaining around 6290 cm^{-1} optical gain from 6 Å InN/12 Å $In_{0.25}Ga_{0.75}N$, the required total current density is around 1900 A/cm^2.

In general, symmetry and asymmetry of the laser structure show similar trends for total current density. Based on Fig. 10, it is found that non-radiative current density has a higher contribution to the total current density. This non-radiative current density also reduces the efficiency of the laser device. For calculating the threshold current density, only the reference structures are considered. The threshold current density can be determined from the optical gain versus the total current density. Therefore, Fig. 13 is presented to illustrate the optical gain behavior of defined structures as a function of total current density. The threshold gains are utilized to calculate the threshold current densities. Figure 13 shows similar trends seen in Fig. 10 for radiative current density. A laser structure with a wider active region has a higher threshold current density. Here, peak optical gain versus total current density is shown for different coefficients related to non-radiative current density components. Comparing the threshold current densities of different structures, it is observed that laser structure with optimum optical performance also needs lower threshold current to operate. Another important observation from Fig. 13 is that the nitride device with a wider active region is more sensitive to the variation

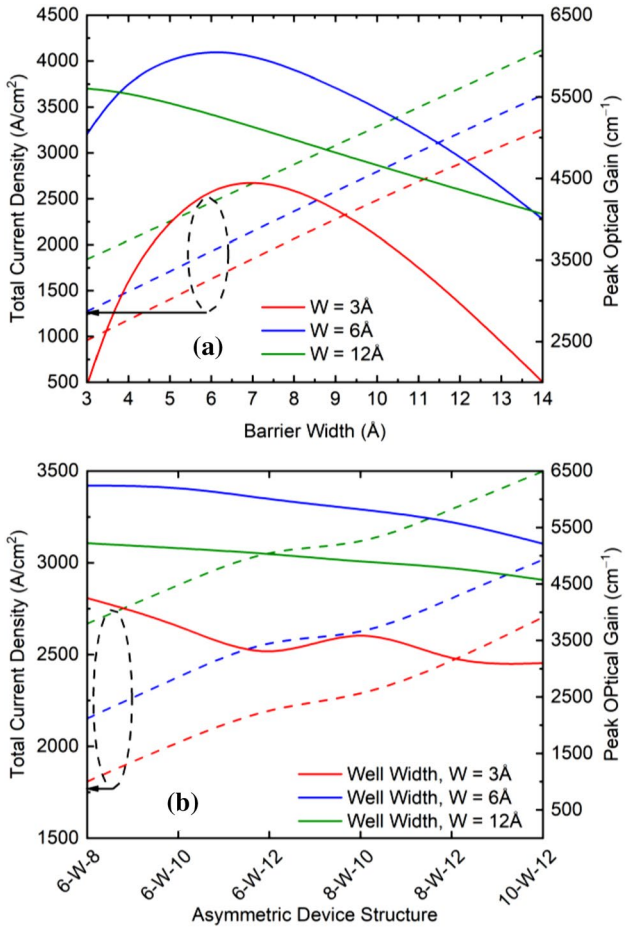

Fig. 12 Total current density and corresponding peak TE-polarized optical gain of **a** symmetric and **b** asymmetric InN/$In_{0.25}Ga_{0.75}$ N QW structure as a function of different barrier structures for well widths of 3 Å, 6 Å, and 9 Å at $T = 300$ K, 5×10^{19} cm^{-3} carrier density, $A = 1 \times 10^9$ s^{-1}, and $C = 1 \times 10^{-31}$ $cm^6 s^{-1}$

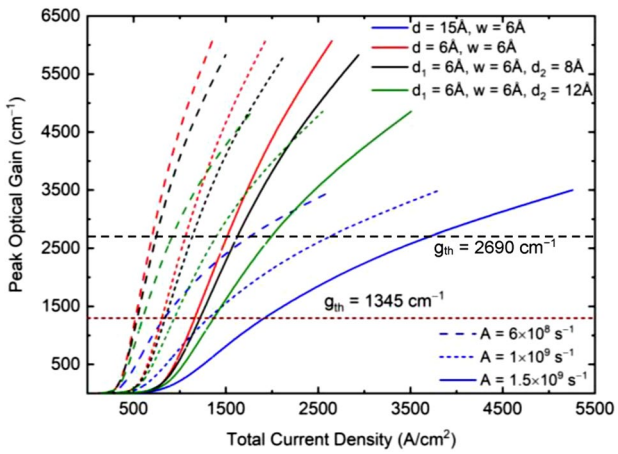

Fig. 13 Peak optical gain versus total current density of different InN/$In_{0.25}Ga_{0.75}$ N QW structure

in optical confinement factor, while the narrower active regions with symmetric and asymmetric barrier layers show less sensitivity to the change in the confinement factor. According to Fig. 13, nitride laser with a narrower active region shows only around 30% increase in threshold current density for a 100% increase in threshold gain. On the other hand, around 80% increase in threshold current density is observed in the wider symmetric laser structure for the 100% increase in threshold gain.

6 Comparison with previous works

To define the improvement achieved in this work, a comparison study is demonstrated with respect to previously published results. Comparison is drawn based on the optical gain, corresponding threshold current density, and emission wavelength. Table 1 shows the state-of-the-art results of different nitride laser structures including polar, semipolar, and nonpolar (Here, in the table, $^{\|}$represents higher carrier concentration, $^{\#}$represents J_{rad}, * represents modal gain, and $^{\dotplus}$represents output power). From the comparison, it is seen that the obtained optical performance from this work is promising. Here, one important drawback is to achieve maximum optical performance at the target operating wavelength. To approach this, suitable material systems need to choose to obtain the target output which is another challenge due to the time required to obtain the optimum device parameters to achieve the target.

7 Genetic algorithm-based optimization

Performing the optimization by considering the multiple variables is always a tedious task. With four variables of the symmetric device, the required time for parameter tuning was around 70.21 h, while completion of the optimization with the asymmetric variation of 6 variables required 294.14 h. Therefore, with the increase in the number of variables, the completion time for optimization in a conventional way is increased almost exponentially. To get a time-efficient optimization process, a genetic algorithm (GA)-based optimization has been also performed in this work to achieve the target result of maximum optical gain. The required time to obtain the same optimization results from the genetic algorithm-based optimization was less than 50% of the prior required time (around 21 h for symmetric tuning and 32 h for asymmetric tuning). Therefore, this optimization process is more time-efficient for the optimization of optical properties of nitride devices with a large number of variables. Genetic-based optimization was performed with the MATLAB optimization toolbox. GA is better than the other available optimization algorithms as GA performs a parallel search for the optimized result. It utilizes the principles of natural evolution: reproduction, selection, and diversity. In this work, multi-objective optimization has been used to optimize the TE and TM optical gain. Negative values of the target functions are used for optimizing the parameters which offer reduced ambiguity and better screening and flexibility in the optimization process.

Table 1 Comparison of polar, semipolar, and nonpolar laser structures

Materials	Type	Optical gain (cm^{-1})	Peak wavelength (nm)	Threshold current (A/cm^2)
InGaN/AlGaInN/GaN [38]	Polar	~2800	~490	1480
InGaN/GaN/AlGaN [39]	Polar	~1000	~470	–
	Semipolar	~4000	~450	–
	Non-polar	~3500	~425	–
GaN/InGaN [40]	Semipolar	~20,000$^{\|}$	~530	~300$^{\#}$
GaN [41]	Polar	~16*	~455	~2480
	Non-polar	~25*	~440	~3240
GaN-based VCSEL [42]	Polar	0.2 mW$^{\dotplus}$	~420	23,000
	Non-polar	1.1 mW	~454	36,000
InN/InGaN/GaN This work	Polar	~6290 (Sym.)	~710	~1100 (Γ_{opt}=0.01) ~1500 (Γ_{opt}=0.005)
		~6220 (Asym.)	~800	~1160 (Γ_{opt}=0.01) ~1600 (Γ_{opt}=0.005)

8 Conclusion

In this work, the wurtzite-nitride-based SQW laser structure is investigated to study the change in electrical and optical properties due to the tuning of device parameters like well width, barrier width, SCH width, and injection carrier density. Device parameter tuning provides an option for band engineering which tunes electron–hole wavefunction overlap factor, and hence, the electronic, optical, and threshold properties of the laser devices. A simulation engine is developed based on theoretical formulations including the incorporation of Hamiltonian and Poisson's Expressions. The aim is to obtain optimum device structure to get maximum optical performance from the band engineering. To achieve the goal, optimization work is performed with both conventional and genetic algorithm-based optimization processes. From the study of the optimization process, the impacts of the device parameters on the electronic and optical properties are demonstrated in detail which can provide a better understanding of modifying the laser device performance by tuning the external parameters. The obtained results are compared with the previously published results to show both validity of this work as well as the improvement of the optical performance.

References

1. T.D. Moustakas, R. Paiella, Optoelectronic device physics and technology of nitride semiconductors from the UV to the terahertz. Rep. Prog. Phys. **80**(10), 106501 (2017)
2. D.N. Faye et al., Study of damage formation and annealing of implanted III-nitride semiconductor for optoelectronic devices. Nucl. Instr. Meth. Phys. Res. B **379**, 251–254 (2016)
3. M. Razeghi, III-nitride optoelectronic devices: from ultraviolet toward terahertz. IEEE Photon. J. **3**(2), 263–267 (2011)
4. J.J. Wierer Jr., J.Y. Tsao, Advantages of III-nitride laser diodes in solid-state lighting. Phys. Status Solidi A **212**(5), 980–985 (2015)
5. C. Weisbuch et al., The efficiency challenge of nitride light-emitting diodes for lighting. Phys. Status Solidi A **212**(5), 899–913 (2015)
6. J.J. Wierer Jr. et al., III-nitride quantum dots for ultra-efficient solid-state lighting. Laser Photonics Rev. **10**(4), 612–622 (2016)
7. H. Ohta, S.P. DenBaars, S. Nakamura, Future of group-III nitride semiconductor green laser diodes. J. Opt. Soc. Am. B **27**(11), B45–B49 (2010)
8. J. Yang et al., Performance of InGaN based green laser diodes improved by using an asymmetric InGaN/InGaN multi-quantum well active region. Opt. Exp. **25**(9), 9595 (2017)
9. J.S. Speck, D.A. Cohen, *Prospects for High Power Nonpolar and Semipolar GaN-Based Laser Diodes* (2015 IEEE High Power Diode Laser and Systems Conference (HPD), Coventry, 2015).
10. H. Masui et al., Nonpolar and semipolar iii-nitride light-emitting diodes: achievements and challenges. IEEE Trans. Electron Devices **57**(1), 88–100 (2010)
11. T. Melo et al., Gain comparison in polar and nonpolar/semipolar gallium-nitride-based laser diodes. Semicond. Sci. Technol. **27**, 024015 (2012)
12. Z.Q. Li, Z.M. Simon Li, J. Piprek, Simulations of laser diodes with nonpolar InGaN multi-quantum-wells. Phys. Status. Solidi C **7**(7–8), 2259–2261 (2010)
13. X. Huang et al., Nonpolar and semipolar InGaN/GaN multiple-quantum-well solar cells with improved carrier collection efficiency. Appl. Phys. Lett. **110**, 161105 (2017)
14. M. Sawicka et al., Comparative study of semipolar (20-1), nonpolar (10-0) and polar (0001) InGaN multi-quantum well structures grown under N- and In-excess by plasma assisted molecular beam epitaxy. J. Crys. Growth **465**, 43–47 (2017)
15. A.M. Smirnov et al., Critical thickness for the formation of misfit dislocations originating from prismatic slip in semipolar and nonpolar III-nitride heterostructures. APL Mater. **4**, 016105 (2016)
16. Y. Zhao et al., Toward ultimate efficiency: progress and prospects on planar and 3D nanostructured nonpolar and semipolar InGaN light-emitting diodes. Adv. Opt. Photon. **10**(1), 246–308 (2018)
17. J. Zhang, N. Tansu, Engineering of AlGaN-delta-GaN quantum-well gain media for Mid- and deep-ultraviolet lasers. IEEE Photon. J. **5**(2), 2600209 (2013)
18. M.M.H. Polash, M.S. Alam, Optical gain optimization of Al0.8Ga0.2N-delta-GaN quantum well laser in ultraviolet spectra using genetic algorithm. ECS Trans. **69**, 81–90 (2015)
19. M.V. Kisin, R.G.W. Brown, H.S. El-Ghoroury, Optimum quantum well width for III-nitride nonpolar and semipolar laser diodes. Appl. Phys. Lett. **94**, 021108 (2009)
20. M.M.H. Polash, K. Khan, Characterization of InN-In0.25Ga0.75N quantum well laser with In0.4Al0.6N Layers for 1300 nm band. MRS Adv. **1**(28), 2051–2057 (2016)
21. M.M.H. Polash, M.S. Alam, S. Biswas, Design and analysis of InN-In0.25Ga0.75N single quantum well laser for short distance communication wavelength. Opt. Eng. **57**, 036110 (2018)
22. A. McAllister, D. Bayerl, E. Kioupakis, Radiative and Auger recombination process in indium nitride. Appl. Phys. Lett. **112**(25), 251108 (2018)
23. H. Zhao et al., Self-consistent analysis of strain-compensated InGaN-AlGaN quantum wells for lasers and light-emitting diodes. IEEE J. Quantum Electron. **45**(1), 66–78 (2009)
24. H. Zhao et al., Optical gain and spontaneous emission of strain-compensated InGaN–AlGaN quantum wells including carrier screening effect. Proc. SPIE **6889**, 688903 (2008)
25. S.L. Chuang, Optical gain of strained wurtzite GaN quantum-well lasers. IEEE J. Quantum Electron. **32**(10), 1791–1800 (1996)
26. S.L. Chuang, *Physics of Optoelectronic Devices* (Wiley, New York, 1995).
27. S.L. Chuang, C.S. Chang, A band-structure model of strained quantum-well wurtzite semiconductors. Semicond. Sci. Technol. **12**(3), 252–263 (1997)
28. P. Harrison, *Quantum Wells, Wires and Dots* (John Wiley & Sons, West Sussex, 2005).
29. O. Ambacher et al., Pyroelectric properties of Al(In)GaN/GaN hetero- and quantum well structures. J. Phys. Condens. Matter. **14**(13), 3399–3434 (2002)
30. W.W. Chow, M. Kneissl, Laser gain properties of AlGaN quantum wells. J. Appl. Phys. **98**, 114502 (2005)
31. P.S. Zory (ed.), *Quantum Well Laser—Principles and Applications* (Academic Press, New York, 1993)
32. H. Zhao, G. Liu, N. Tansu, Analysis of InGaN-delta-InN quantum wells for light-emitting diodes. Appl. Phys. Lett. **97**, 131114 (2010)
33. H. Luth et al., "InGaN mesoscopic structures for low energy consumption nano-optoelectronics," in *2016 11th International Conference on Advanced Semiconductor Devices Microsystems (ASDAM)*, Smolenice, Slovakia, pp. 69–72 (2016)
34. M.M.H. Polash, M.S. Alam, Characterization of InN-In0.25Ga0.75N quantum well laser structure for 1330 nm. ECS Trans. **69**(12), 71–80 (2015)
35. J. Hader et al., Nitride semiconductor devices, J. Piprek, Ed. Wiley-CCH, Weinheim, Germany (2007)

36. J. Hader et al., On the importance of radiative and Auger losses in GaN-based quantum wells. Appl. Phys. Lett. **92**(26), 261103 (2008)
37. K.T. Delaney, P. Rinke, C.G. Van de Walle, Auger recombination rates in nitrides from first principles. Appl. Phys. Lett. **94**(19), 191109 (2009)
38. H. Fu, W. Sun et al., Gain characteristics of InGaN quantum wells with AlGaInN barriers. AIP Adv. **9**, 045013 (2019)
39. W.W.G. Scheibenzuber et al., Calculation of optical eigenmodes and gain in semipolar and nonpolar InGaN/GaN laser diodes. Phys. Rev. B **80**(11), 115320 (2009)
40. S.-H. Park, D. Ahn, Nonpolar and semipolar GaN, optical gain and efficiency. Proc. SPIE **8625**, 862511 (2013)
41. T. Melo et al., Gain comparison in polar and nonpolar/semipolar gallium-nitride-based laser diodes. Semicond. Sci. Technol. **27**(2), 024015 (2012)
42. M. Monavarian, A. Rashidi, D. Feezell, A decade of nonpolar and semipolar III-nitrides: a review of successes and challenges. Phys. Status Solidi A **216**(1), 1800628 (2019)